INORGANIC CHEMISTRY FRONTIERS

RESEARCH ARTICLE

View Article Online
View Journal | View Issue

Cite this: *Inorg. Chem. Front.*, 2022, **9**, 3148

Precursor-converted formation of bimetallic–organic framework nanosheets for efficient oxygen evolution reaction†

Lei Xia,[a,b] Crystal Bowers,[c] Pei Dong,[c] Mingxin Ye *[a] and Jianfeng Shen*[a]

Received 16th January 2022,
Accepted 28th April 2022

DOI: 10.1039/d2qi00133k

rsc.li/frontiers-inorganic

The design and preparation of outstanding catalysts are significant for the electrocatalytic oxygen evolution reaction (OER), which performs a crucial function in electrochemical water splitting. Herein, we have prepared metal–organic framework (MOF) nanosheets on a nickel foam (NF) substrate *via* a two-step procedure including a hydrothermal reaction and an *in situ* transformation process. As for the anodic OER process, the obtained NiFe-MOF@NF demonstrates excellent catalytic performance with a small overpotential of 265 mV to reach a current density of 10 mA cm^{-2}, and impressive long-term catalytic durability and stability without obvious deactivation. The superior electrocatalytic performance of the obtained NiFe-MOF@NF material is mainly due to the substantial active metal centres, enhanced electrical conductivity and favorable kinetics. We believe that the strategy will be of great benefit to the development of highly efficient metal electrocatalysts, and will pave the way for the application of metal catalysts in the OER.

Introduction

The increasing depletion of carbon-based fuels, including coal, petroleum and natural gas, has caused adverse effects on the environment, such as global warming and atmospheric pollution.[1] These growing environmental concerns have prompted researchers to pursue clean and sustainable energy to substitute non-renewable fossil fuels.[2] Hydrogen (H_2) enjoys the advantage of an extremely high gravimetric energy density (120–140 MJ kg^{-1}),[3] and its combustion by-product is merely pollution-free water.[4] Owing to these excellent features, H_2 is proposed as one of the most potential substitutes for future low-carbon systems. Water electrolysis is considered as a prospective strategy to efficiently produce H_2. During the water electrolysis process, renewable electricity is converted into storable and transportable chemical fuel with no greenhouse gas emission.[5,6] However, the anodic oxygen evolution reaction (OER), involving four sequential electron transfer pathways, is an uphill process featuring inherently sluggish kinetics,[7,8] which is a bottleneck for H_2 energy production in electrocatalytic water splitting.[9] The electrocatalyst can effectively overcome the kinetic barrier of the OER process.[10,11] Precious metal oxides (*e.g.* IrO_2 and RuO_2) have been used as the electrocatalysts for the OER.[12,13] Unfortunately, their scaled-up commercial application is rigorously impeded by their low-reserves and high price.[14,15] Consequently, the fabrication of efficient and robust OER electrocatalysts consisting of Earth-abundant elements is of primary importance for water electrolysis.

As a considerably novel type of porous material, metal–organic frameworks (MOFs), comprising metal centres linked by organic ligands, possess numerous advantages of ultrahigh internal surface area,[16] chemical modularity,[17] uniform and adjustable porous structures,[18] and accurate designability.[19] These intrinsic features endow MOFs with great potential in a large variety of disciplines, including gas separation,[20] biomedical delivery,[21] chemical sensors,[22] and energy conversion and storage.[23] Nevertheless, most of the pristine MOFs are usually bulk materials suffering from the obstruction of active metal sites by surrounding organic ligands and low electrical conductivity,[24] which dramatically hinder their utilization as electrode materials. Calcination at high temperature has been reported to effectively improve the conductivity of MOFs.[25] Notably, the pyrolysis treatment usually results in the degradation of organic ligands and aggregation of metal centres, which will destroy the structure thoroughly and sacrifice intrinsic metal active sites.[26,27] From a structural point of view, well-designed MOF catalysts could possibly converge the strengths of homo- and heterogeneous catalysts,[28] which can

[a]*Institute of Special Materials and Technology, Fudan University, Shanghai 200433, China. E-mail: mxye@fudan.edu.cn, jfshen@fudan.edu*
[b]*Department of Chemistry, Fudan University, Shanghai 200433, China*
[c]*Department of Mechanical Engineering, George Mason University, VA 22030, USA*
†Electronic supplementary information (ESI) available. See DOI: https://doi.org/10.1039/d2qi00133k

achieve direct utilization as high-performance OER electrocatalysts without a further pyrolysis process. Due to the unique morphology of two-dimensional (2D) materials, 2D MOF nanosheets have garnered increasing research interest recently. The OER may benefit from 2D ultrathin sheet-like structures due to their following merits: nanometre thickness accelerates mass transport and electron transfer,[29] high exposure of catalytically active surfaces offers more accessible active metal sites,[30] and surface coordinative unsaturated metal sites facilitate the interaction with substrate molecules,[31] all of which perfectly cater to the requirements of an excellent OER catalyst.

A liquid-phase exfoliation strategy is utilized to synthesize 2D MOF nanosheets. Usually, it needs consecutive ultrasonication for a long time, accompanied by structural destruction, morphological distortion, restacking of the formed MOF nanosheets and low production rates.[32,33] Besides, the exfoliation method is only applicable to layered MOFs with weak interlayer interactions. On the other hand, MOF nanosheets can also be prepared *via* a surfactant-assisted synthetic method. Nevertheless, it is not easy to completely remove the organic surfactant, which may bind on the surface of MOF nanosheets and partially block the active sites.[34]

Herein, we have adopted an *in situ* transformation method to synthesize 2D NiFe-MOF nanosheets on nickel foam (NiFe-MOF@NF), which involves a facile hydrothermal growth of layered double hydroxide (LDH) and ligand exchange under solvothermal conditions. Compared to the above methods, a precursor-converted strategy can avoid the use of organic modulators and provide abundant active sites. Moreover, a self-supporting electrode can be easily fabricated through this strategy, which is beneficial for practical application. With the merits of accessible active metal centres and enhanced charge transfer, the as-prepared NiFe-MOF@NF exhibits kinetic activity with a superior OER overpotential of 265 mV (10 mA cm^{-2}), a small Tafel slope (38.1 mV dec^{-1}) and robust stability in alkaline media.

Experimental section

Materials

Iron(III) nitrate nonahydrate ($Fe(NO_3)_3{\cdot}9H_2O$, ≥98.5%), ammonium fluoride (NH_4F, ≥99.5%), *N,N*-dimethylmethanamide (DMF, ≥99.5%), hydrochloric acid (HCl, ≈37 wt%) and ethanol (C_2H_5OH, ≥95%) were bought from Sinopharm Chemical Reagent Co., Ltd. Potassium hydroxide (KOH, ≥85%) was purchased from Shanghai Lingfeng Chemical Reagent Co., Ltd. Urea ($CO(NH_2)_2$, 99%), *p*-phthalic acid (PTA, 99%) and commercial RuO_2 were bought from Shanghai Aladdin Bio-Chem Technology Co., Ltd. Deionized (DI) water was purified with a Ulupure device. These chemical reagents were directly used in this experiment without further purification.

Preparation of NiFe-LDH@NF

$Fe(NO_3)_3{\cdot}9H_2O$ (0.5 mmol, 200 mg), NH_4F (2 mmol, 74 mg) and urea (5 mmol, 300 mg) were dissolved in deionized (DI) water (15 mL) to form a clear solution under stirring conditions. NF (about 2 cm × 3 cm) was pretreated with 3 M HCl solution under ultrasonic conditions for 10 min to remove the surface oxide and then rinsed with DI water and absolute ethanol for 10 min each time. Subsequently, the above solution and pretreated NF were placed into a 20 mL Teflon-lined stainless-steel autoclave, which was maintained at 120 °C for 6 h. After the reactor cooled down to room temperature naturally, the NiFe-LDH@NF was collected and rinsed thoroughly with DI water and dried in an oven at 65 °C for 12 h.

Preparation of NiFe-MOF@NF

Typically, PTA (50 mg) was dissolved in DMF (12 mL) and stirred to obtain a clear solution. Subsequently, the resultant solution was put into a 20 mL autoclave, followed by immersing a piece of the NiFe-LDH@NF material (1 × 2 cm). Afterward, the autoclave was maintained at 180 °C for 6 h. After natural cooling to room temperature, the NiFe-MOH@NF was taken out and rinsed with water under sonication for 10 s, and then washed with DI water three times, and dried in an oven at 65 °C for 12 h.

Preparation of RuO_2@NF

10 mg RuO_2, 300 μL DI water, 350 μL ethanol and 50 μL 5% Nafion were mixed and dispersed under ultrasonic conditions for 0.5 h. Then, 200 μL RuO_2 ink was coated on NF (1 cm × 0.5 cm).

Physicochemical characterization

The morphological features of the materials were characterized using scanning electron microscopy (SEM, Tescan, MAIA3 XMH, 15 kV) and high-resolution transmission electron microscopy (HRTEM, JEM-2100, 200 kV). Before the TEM test, a small piece of NiFe-MOF@NF was uniformly dispersed in ethanol *via* ultrasonication for 30 min. The crystalline structure of the samples was investigated by X-ray diffraction (XRD) using a Bruker D8 Advanced X-ray diffractometer with Cu Kα radiation (λ = 0.154 nm, tube power: 40 kV, 40 mA). Fourier transform infrared (FT-IR) spectra were recorded in a range of 400 to 4000 cm^{-1} using Nicolet Is10. The surface chemistry of the materials was investigated by X-ray photoelectron spectroscopy (XPS, Thermo Scientific K-Alpha) correcting with adventitious carbon (C 1s) at 284.8 eV. Raman measurements were conducted using a HORIBA Scientific LabRAM HR Evolution device with 633 nm wavelength incident laser light.

Electrochemical measurements

All electrochemical tests were conducted using a CHI 760E Electrochemical Workstation (Shanghai Chenhua Instrument Corp., China) under ambient conditions with a 1 M KOH electrolyte. Materials on the NF (0.5 cm × 0.5 cm) served as a working electrode. A polished graphite rod was selected to act as a counter electrode, and a saturated calomel electrode (SCE) was used as the reference electrode. Potentials were calibrated with a reversible hydrogen electrode (RHE) according to the Nernst equation: $E_{RHE} = E_{SCE} + 0.242 + 0.059 \times pH$. Linear

sweep voltammetry (LSV) was performed under a small scan rate of 5 mV s^{-1}. The overpotential (η) for OER measurements was obtained based on the formula: $\eta = E_{RHE} - 1.23$. Tafel curves were extracted from the LSV according to the Tafel equation ($\eta = b \log j + a$),[35] where j refers to the current density, and b stands for the Tafel slope, respectively. Thus, the Tafel slopes were obtained from the corresponding LSV data *via* plotting η against $\log(j)$. The electrochemically active surface area (ECSA) of the samples was examined using the double-layer capacitance (C_{dl}), which was measured using cyclic voltammetry (CV) in a non-faradaic range 0–0.1 V (*versus* SCE) at various scan rates (v = 10, 20, 40, 60, 80 and 100 mV s^{-1}). The C_{dl} was estimated $\Delta j = (j_{anodic} - j_{cathodic}$ charge) at 0.05 V (*versus* SCE) against the scan rates. To evaluate the durability of the working electrode, chronoamperometric (i–t) tests were carried out at different current densities of 10, 50 and 100 mA cm^{-2} for 10 h each time. Additionally, 2000 cycles of CV between 0 and 0.4 V (*vs.* SCE) were conducted at 60 mV s^{-1} before the i–t measurements. Electrochemical impedance spectroscopy (EIS) measurements were performed under the following conditions: a frequency region of 0.1–10^5 Hz and an amplitude of 10 mV.

Results and discussion

The present NiFe-MOF@NF material was prepared *via* a two-step growth procedure including a hydrothermal synthesis and a solvothermal transformation, as shown in Fig. 1. The synthesis of NiFe-LDH@NF included the precipitation of Fe and Ni ions on NF in an aqueous system, which was induced by urea and NH_4F. The source of Fe ions was from the added salt reactant, while the Ni ions were leached out from the NF substrate. During this synthesis process, urea progressively decomposed into NH_3 and CO_3^{2-}. The slow release of NH_3 provides weakly basic conditions[36] and leads to homogeneous nucleation and crystallization of LDH materials.[37] Serving as the intercalated anion, CO_3^{2-} is prone to adsorb on the (001) surface. Consequently, the growth of planes alongside the [001] orientation is restricted.[38] In addition, NH_4F is found to be beneficial for the growth of nanosheets by reducing the nucleation rate and activating the substrate. F^- will coordinate with Fe ions first, so the Fe ions will be released slowly into the reaction system, promoting the formation of NiFe-LDH on the substrate rather than in the liquid solution.[39] The supersaturation of Ni and Fe ions can be remarkably inhibited by the effective coordination with F^- ions or NH_3, which results in a substantial reduction in the concentrations of Fe and Ni ions in the solution.[40] Thus, the Fe and Ni ions will be gradually released into the reaction solution under a low supersaturation system, which facilitates the growth of NiFe-LDH nanosheets.[41]

Then, in a ligand exchange reaction, NiFe-LDH not only acts as the template to fabricate the nanosheet morphology but also serves as a self-sacrificial precursor to offer Fe and Ni ions for the formation of NiFe-MOF. During this step, H^+ ions and PTA groups originate from the hydrolysis of PTA ligands, and the deprotonated H^+ gradually reacts with the NiFe-LDH precursor and releases Ni and Fe ions, which immediately coordinate with PTA groups. Ultimately, the NiFe-LDH@NF is completely transformed into NiFe-MOF@NF owing to the slow dissolution of LDH caused by H^+ and the *in situ* rapid chelation of PTA ligands with metal ions.[42,43]

The SEM image of NiFe-LDH@NF (Fig. 2a) exhibits a hierarchical structure with interconnected nanosheets. As for NiFe-MOF@NF, the SEM image (Fig. 2b) illustrates that it inherits a sheet-like morphology after the solvothermal transformation reaction. The XRD pattern proves that NiFe-LDH (Fig. 2c) was successfully synthesized, and all characteristic peaks coincide well with hexagonal $Fe_2Ni_2(CO_3)(OH)_8{\cdot}nH_2O$ (JCPDS: 49-0188). The peaks at 11.7°, 23.4°, 34.4°, 39.1°, 46.7°, 60° and 61.3° are indexed as (003), (006), (012), (015), (018), (110) and (113), respectively. The intensities of the (00l) planes decrease as l increases, which are characteristic of layered double hydroxides.[44] Notably, three conspicuous diffraction peaks (marked "Δ") at 44.6°, 51.8° and 76.4° in NiFe-LDH@NF belong to Ni (JCPDS: 04-0850), originating from the NF. Moreover, the main (003) diffraction peak at a 2θ value of 11.7° indicates the presence of intercalated CO_3^{2-} in the NiFe-

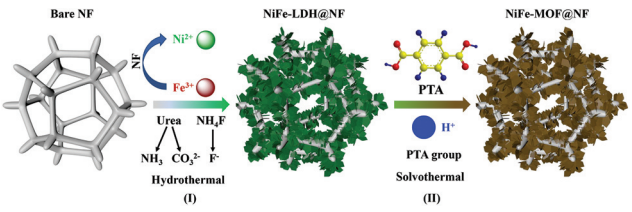

Fig. 1 Synthetic scheme of NiFe-MOF@NF. (I) Hydrothermal synthesis of NiFe-LDH@NF and (II) *in situ* transformation into NiFe-MOF@NF through a solvothermal reaction.

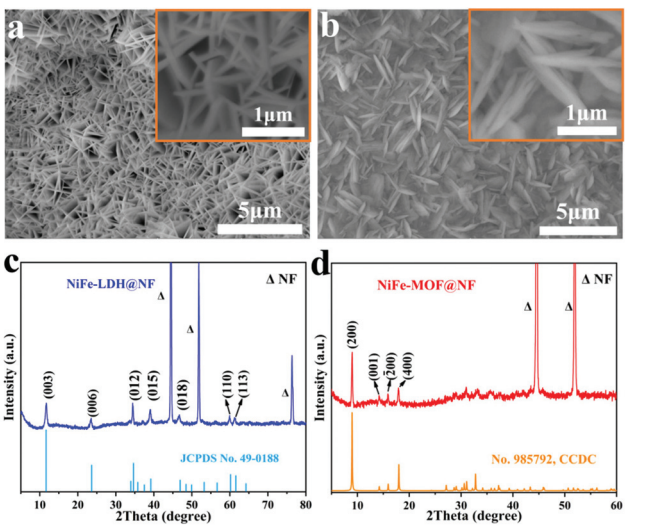

Fig. 2 SEM images of (a) NiFe-LDH@NF and (b) NiFe-MOF@NF (the inset shows high magnification SEM images). XRD data of (c) NiFe-LDH@NF and (d) NiFe-MOF@NF.

LDH.[45,46] After the transformation, the XRD pattern indicates that the crystalline phase of NiFe-MOF (Fig. 2d) is isostructural to the Ni-based MOF (no. 985 792, $Ni_2(OH)_2(C_8H_4O_4)$, Cambridge Crystallographic Data Centre).[47] The diffraction peak at 8.9° is assigned to the (200) crystal planes. The Ni and Fe atoms in the outermost MOF layer are preferred to produce unsaturated coordination metal centres with unexpected electrocatalytic properties.[48]

The morphology and structure were also proved by TEM as shown in Fig. 3a. The NiFe-MOF detached from the NF substrate (more details in the Experimental section) consists of nanosheets. The HR-TEM image (Fig. 3b) exhibits a lattice spacing of 0.995 nm corresponding to the (200) plane of NiFe-MOF. In addition, energy-dispersive X-ray spectroscopy (EDS) in STEM mode indicates uniform distributions of C, O, Ni and Fe elements in the NiFe-MOF (Fig. 3c and d).

To further identify the complete conversion of the NiFe-LDH to NiFe-MOF, FT-IR spectroscopy was performed. The FT-IR spectrum of pristine NiFe-LDH in Fig. 4a shows a weak peak at 1612 cm^{-1}, which is characteristic of the bending vibration mode of water molecules, and two strong peaks at 1356 and 774 cm^{-1} belong to the ν_3 stretching and bending vibration modes of intercalated CO_3^{2-}, respectively.[49] The FT-IR spectrum indicates the presence of intercalated CO_3^{2-}, –OH, and water molecules, matching with the XRD pattern of NiFe-LDH@NF. As for PTA-based MOF materials, the spectral split between the symmetric and antisymmetric stretching vibration modes of the carboxylate group (–COO–) is slightly higher than 200 cm^{-1}.[50] This characteristic helps in the assignment of the as-obtained NiFe-MOF. The peak at 3602 cm^{-1} is assigned to the stretching vibrations of OH–, and the band at 1498 cm^{-1} belongs to *para*-aromatic C–H groups.[29] PTA powder exhibits the ν_{as} (–COO–) at 1682 cm^{-1}, which disappears in NiFe-MOF. Instead, two new bands are visible at 1583 and 1359 cm^{-1} attributed to the ν_{as} (–COO–) and ν_s (–COO–) with a split of 224 cm^{-1}. All the above analyses prove the coordination of metal ions with PTA ligands in the NiFe-MOF. Notably, the carboxylate groups exposed on the surface will make the NiFe-MOF@NF catalyst hydrophilic, which would facilitate the adsorption and dissociation of water during the OER process.[51]

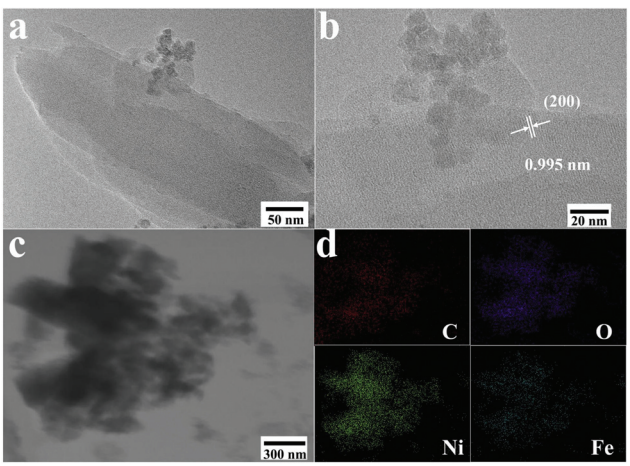

Fig. 3 (a) TEM, (b) HR-TEM and (c) STEM images of the NiFe-MOF catalyst. (d) EDX elemental mappings in the NiFe-MOF catalyst.

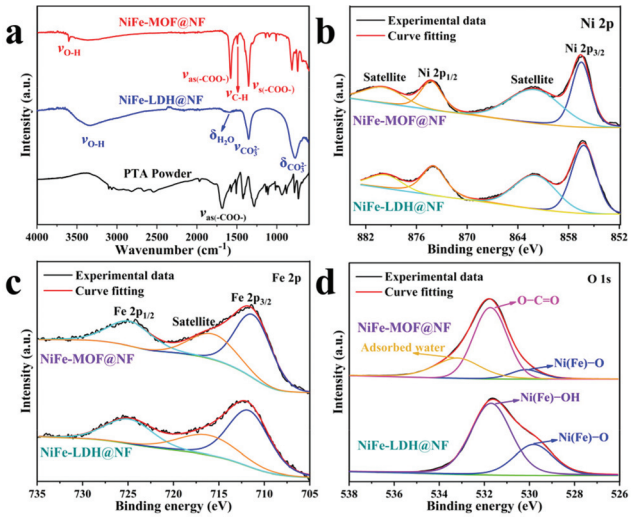

Fig. 4 (a) FT-IR of PTA powder, NiFe-LDH@NF and NiFe-MOF@NF. High-resolution XPS patterns of (b) Ni 2p, (c) Fe 2p and (d) O 1s spectra in NiFe-LDH@NF and NiFe-MOF@NF.

We also investigated the morphological and structural evolution of NiFe-MOF at different reaction times through SEM images, XRD patterns and FT-IR spectra (Fig. S1 and S2†). It can be concluded that the NiFe-LDH was completely transformed into NiFe-MOF after a 6 h ligand exchange reaction. Moreover, Raman measurements were also conducted to characterize the NiFe-MOF@NF material. In Fig. S3,† the as-obtained NiFe-MOF@NF shows a doublet at around 1612 and 1422 cm^{-1} attributed to the in- and out-of-phase stretching vibration modes of the –COO– group.[52] Additionally, the peak at 1134 cm^{-1} probably associates with a deformation mode involving the –COO– coupled with a C–C stretching mode, and two peaks at around 861and 691 cm^{-1} belong to the benzene ring stretching vibration mode corresponding to C–H.[53] At lower Raman shifts, two bands at 478 and 566 cm^{-1} are attributed to the M–O (M = Ni^{2+}/Fe^{3+}) bands.[25]

Furthermore, XPS was conducted to analyze the surface electronic state. The full survey patterns (Fig. S4†) indicate the presence of C, O, Ni and Fe elements. It should be noted that there are some remaining F elements in NiFe-LDH albeit with a thorough wash with water during preparation. The high-resolution XPS spectra of samples were employed to study the chemical valences of Ni and Fe ions and the types of oxygen species. The Ni 2p spectra (Fig. 4b) show two spin–orbit peaks at around 874 and 856 eV, with two weak satellite peaks at around 880 and 860 eV, respectively, indicating the Ni^{2+} oxidation state in both samples.[54,55] As to the spectra of Fe 2p (Fig. 4c), the observation of Fe $2p_{3/2}$ and Fe $2p_{1/2}$ at ~712 and ~725 eV matches well with the characteristics of Fe^{3+} oxidation states.[56,57] With regard to the O 1s spectrum (Fig. 4d), NiFe-

LDH@NF presents two peaks at 531.4 and 529.5 eV, belonging to Ni(Fe)–OH and Ni(Fe)–O species, respectively.[58,59] As for the NiFe-MOF@NF catalyst, its O 1s spectrum involves three peaks at 530.2, 531.7 and 533.2 eV assigned to the Ni(Fe)–O species, the –COO– groups of PTA ligands and absorbed water, respectively.[51,60] NiFe-MOF possesses a higher content of surface absorbed water compared to NiFe-LDH, which may provide more accessible active sites during the electrolysis process. Moreover, these hydrophilic compounds (water and carbonate groups) induce a better hydrophilic surface, which can be more favorable to the OER.[61]

Linear sweep voltammetry (LSV) was conducted to acquire polarization curves of the NF substrate, NiFe-LDH@NF, NiFe-MOF@NF and commercial RuO_2@NF electrodes. In the LSV curve, the anodic peak at 1.43 V (*vs.* RHE) is attributed to the oxidation of Ni^{2+} to Ni^{3+} in alkaline solution. According to the LSV in Fig. 5a, b and Fig. S5a† (the reverse scan of LSV from the positive to negative potential), NiFe-MOF@NF only needs a small overpotential of 265 mV to reach the current density of 10 mA cm^{-2}, which is much smaller in relation to other controlled samples, including commercial RuO_2@NF (305 mV), NiFe-LDH@NF (317 mV) and NF (388 mV). Moreover, the superior OER catalytic performance of the NiFe-MOF@NF catalyst is indicated by a smaller Tafel plot extracted from LSV (38.1 mV dec^{-1}, Fig. 5c) compared to other catalysts such as the NF substrate (93 mV dec^{-1}), pristine NiFe-LDH (71.4 mV dec^{-1}), and commercial RuO_2 (84.1 mV dec^{-1}), which clarifies a fast charge-transfer kinetics of NiFe-MOF@NF. This value is close to that obtained from the steady state measurements (43 mV dec^{-1} for NiFe-MOF@NF, Fig. S5b†). The comparison of the OER performance with those of similar catalysts is listed in Table S1.†

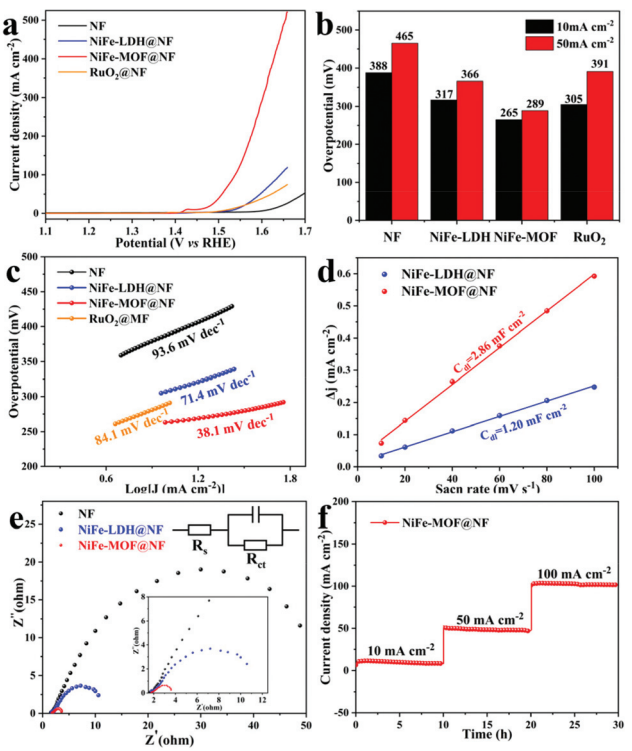

Fig. 5 (a) LSV of the obtained samples. (b) The overpotentials of samples at different current densities of 10 and 50 mA cm^{-2}. (c) Tafel plots of the samples. (d) The C_{dl} of NiFe-LDH@NF and NiFe-MOF@NF. (e) The EIS curves of NF, NiFe-LDH@NF and NiFe-MOF@NF. (f) The durability test of NiFe-MOF@NF.

ECSA and EIS measurements were carried out to explore the possible reasons for the enhanced electrocatalytic performance after the conversion. On one hand, the nanosheet morphology gives rise to more active centres. In order to testify this hypothesis, the C_{dl} values of these samples were estimated to evaluate the ECSA, which is related to the active sites of electrocatalysts and is generally proportional to the C_{dl} (Fig. S6†). The results (Fig. 5d) show that the NiFe-MOF@NF shows the highest C_{dl} of 2.86 mF cm^{-2}, which is larger than that of NiFe-LDH@NF (1.2 mF cm^{-2}) demonstrating that the higher OER performance could be related to the augmentation of the ECSA, which associates with the active centres. On the other hand, EIS curves were measured to investigate the interfacial properties and the superior OER reaction kinetics of the electrodes. EIS tests of all samples were conducted at 0.5 V (*versus* SCE). The EIS curves with a fitting equivalent circuit model for different samples are illustrated in Fig. 5e. The semicircle diameter, which stands for the charge transfer resistance (R_{ct}) value of NiFe-MOF@NF (1.9 Ω), is smaller than those of NiFe-LDH@NF (10.4 Ω) and NF (54.9 Ω), demonstrating a faster intrinsic charge transfer of NiFe-MOF@NF than the other two electrodes. The improvement of conductivity is generally due to 2D nano-structuration that can induce vacancy engineering inside the NiFe-MOF nanosheet. These vacancies can act as shallow donors to increase the carrier concentration of the metal octahedral units ($NiFeO_6$) of the NiFe-MOF, thereby enhancing its conductivity.[35] The substantial active centres, efficient charge transport and enhanced electrical conductivity consequently endow NiFe-MOF@NF with high catalytic activity.

Besides the excellent activity, the long-term robustness and stability of the electrode for the OER are crucial criteria for evaluating the performance of the electrocatalysis electrodes. To test the durability of NiFe-MOF@NF, 2000 cycles of CV scanning were carried out (0–0.4 V *versus* SCE, 60 mV s^{-1}). After the cycling, the LSV result was similar to the fresh one, with a slight degradation in the current density (Fig. S7†). Meanwhile, the stability of NiFe-MOF@NF was also evaluated by *i–t* measurements (Fig. 5f). Note that the NiFe-MOF@NF electrocatalyst could maintain the current densities for 30 h with little loss. The SEM image of the electrocatalyst after the durability test shows that the nanosheet morphology is preserved well (Fig. S8†). All these results could further prove the durability of the NiFe-MOF@NF material.

In order to unravel the active species, we conducted the XPS analysis of post-NiFe-MOF@NF, as shown in Fig. S9 and S10.† The proportion of Ni^{3+} increases after the durability test, which indicates that surface NiOOH is probably formed during the OER process as the active species.[62]

Based on the results of the experiments, we propose some possible explanations for the stability and enhanced performance of the NiFe-MOF@NF electrocatalyst. Firstly, the loosely coordinated water of the NiFe-MOF can be released in the electrocatalytic OER process to provide catalytic sites. Secondly, the nanosheet structure of the NiFe-MOF exposes more active metal centres and accelerates the mass transfer, which can prevent the overgrowth of bubbles. Finally, the *in situ* formation method endows the NiFe-MOF nanosheets with a strong interaction with the conductive substrate, which lessens the contact resistances and improves the mechanical stability to tackle bubble-induced strains.

Conclusions

In conclusion, this work adopts a precursor-converted strategy to fabricate 2D NiFe-MOF nanosheets supported on the NF substrate, which possess many intriguing features, such as a faster charge transfer and mass transport, an improvement in mechanical stability, and more accessible active centres. Thanks to these advantageous properties, the resulting NiFe-MOF electrode exhibits significantly enhanced catalytic activity with an overpotential of 265 mV (10 mA cm^{-2}), a small Tafel slope (38.1 mV dec^{-1}) and outstanding durability towards the electrocatalytic OER. In consideration of the large variety of LDH precursors, we anticipate that such a method can be conveniently extended to develop other metal-based 2D MOF catalysts for electrochemical energy conversion.

Conflicts of interest

There are no conflicts to declare.

Acknowledgements

The authors acknowledge support from National Natural Science Foundation of China (51972064).

References

1 A. Noori, M. F. El-Kady, M. S. Rahmanifar, R. B. Kaner and M. F. Mousavi, Towards establishing standard performance metrics for batteries, supercapacitors and beyond, *Chem. Soc. Rev.*, 2019, **48**, 1272–1341.
2 N. T. Suen, S. F. Hung, Q. Quan, N. Zhang, Y. J. Xu and H. M. Chen, Electrocatalysis for the oxygen evolution reaction: recent development and future perspectives, *Chem. Soc. Rev.*, 2017, **46**, 337–365.
3 C. Cui, R. Cheng, H. Zhang, C. Zhang, Y. Ma, C. Shi, B. Fan, H. Wang and X. Wang, Ultrastable MXene@Pt/SWCNTs' Nanocatalysts for Hydrogen Evolution Reaction, *Adv. Funct. Mater.*, 2020, **30**, 2000693.
4 S. Roy, Z. Huang, A. Bhunia, A. Castner, A. K. Gupta, X. Zou and S. Ott, Electrocatalytic Hydrogen Evolution from a Cobaloxime-Based Metal-Organic Framework Thin Film, *J. Am. Chem. Soc.*, 2019, **141**, 15942–15950.
5 C. Feng, M. B. Faheem, J. Fu, Y. Xiao, C. Li and Y. Li, Fe-Based Electrocatalysts for Oxygen Evolution Reaction: Progress and Perspectives, *ACS Catal.*, 2020, **10**, 4019–4047.
6 J. Wang, Y. Gao, H. Kong, J. Kim, S. Choi, F. Ciucci, Y. Hao, S. Yang, Z. Shao and J. Lim, Non-precious-metal catalysts for alkaline water electrolysis: operando characterizations, theoretical calculations, and recent advances, *Chem. Soc. Rev.*, 2020, **49**, 9154–9196.
7 Y. J. Son, K. Kawashima, B. R. Wygant, C. H. Lam, J. N. Burrow, H. Celio, A. Dolocan, J. G. Ekerdt and C. B. Mullins, Anodized Nickel Foam for Oxygen Evolution Reaction in Fe-Free and Unpurified Alkaline Electrolytes at High Current Densities, *ACS Nano*, 2021, **15**, 3468–3480.
8 S. Jin, Are Metal Chalcogenides, Nitrides, and Phosphides Oxygen Evolution Catalysts or Bifunctional Catalysts?, *ACS Energy Lett.*, 2017, **2**, 1937–1938.
9 M. Tahir, L. Pan, F. Idrees, X. Zhang, L. Wang, J.-J. Zou and Z. L. Wang, Electrocatalytic oxygen evolution reaction for energy conversion and storage: A comprehensive review, *Nano Energy*, 2017, **37**, 136–157.
10 Y.-C. Zhang, C. Han, J. Gao, L. Pan, J. Wu, X.-D. Zhu and J.-J. Zou, NiCo-Based Electrocatalysts for the Alkaline Oxygen Evolution Reaction: A Review, *ACS Catal.*, 2021, **11**, 12485–12509.
11 K. Zhu, F. Shi, X. Zhu and W. Yang, The roles of oxygen vacancies in electrocatalytic oxygen evolution reaction, *Nano Energy*, 2020, **73**, 104761.
12 F. Gao, Y. Zhang, Z. Wu, H. You and Y. Du, Universal strategies to multi-dimensional noble-metal-based catalysts for electrocatalysis, *Coord. Chem. Rev.*, 2021, **436**, 213825.
13 L. Han, S. Dong and E. Wang, Transition-Metal (Co, Ni, and Fe)-Based Electrocatalysts for the Water Oxidation Reaction, *Adv. Mater.*, 2016, **28**, 9266–9291.
14 R. Zhang, G. van Straaten, V. di Palma, G. Zafeiropoulos, M. C. M. van de Sanden, W. M. M. Kessels, M. N. Tsampas and M. Creatore, Electrochemical Activation of Atomic Layer-Deposited Cobalt Phosphate Electrocatalysts for Water Oxidation, *ACS Catal.*, 2021, **11**, 2774–2785.
15 S. A. Chala, M. C. Tsai, B. W. Olbasa, K. Lakshmanan, W. H. Huang, W. N. Su, Y. F. Liao, J. F. Lee, H. Dai and B. J. Hwang, Tuning Dynamically Formed Active Phases and Catalytic Mechanisms of In Situ Electrochemically Activated Layered Double Hydroxide for Oxygen Evolution Reaction, *ACS Nano*, 2021, **15**, 14996–15006.
16 Q.-L. Zhu, W. Xia, L.-R. Zheng, R. Zou, Z. Liu and Q. Xu, Atomically Dispersed Fe/N-Doped Hierarchical Carbon Architectures Derived from a Metal–Organic Framework Composite for Extremely Efficient Electrocatalysis, *ACS Energy Lett.*, 2017, **2**, 504–511.
17 K. Ikigaki, K. Okada, Y. Tokudome, T. Toyao, P. Falcaro, C. J. Doonan and M. Takahashi, MOF-on-MOF: Oriented

Growth of Multiple Layered Thin Films of Metal-Organic Frameworks, *Angew. Chem., Int. Ed.*, 2019, **58**, 6886–6890.
18 Y. Niu, Y. Yuan, Q. Zhang, F. Chang, L. Yang, Z. Chen and Z. Bai, Morphology-controlled synthesis of metal-organic frameworks derived lattice plane-altered iron oxide for efficient trifunctional electrocatalysts, *Nano Energy*, 2021, **82**, 105699.
19 M. Chang, Y. Wei, D. Liu, J. X. Wang and J. F. Chen, A General Strategy for Instantaneous and Continuous Synthesis of Ultrasmall Metal-Organic Framework Nanoparticles, *Angew. Chem., Int. Ed.*, 2021, **60**, 26390–26396.
20 H. Li, K. Wang, Y. Sun, C. T. Lollar, J. Li and H.-C. Zhou, Recent advances in gas storage and separation using metal–organic frameworks, *Mater. Today*, 2018, **21**, 108–121.
21 A. Kirchon, L. Feng, H. F. Drake, E. A. Joseph and H. C. Zhou, From fundamentals to applications: a toolbox for robust and multifunctional MOF materials, *Chem. Soc. Rev.*, 2018, **47**, 8611–8638.
22 Z. Liang, C. Qu, W. Guo, R. Zou and Q. Xu, Pristine Metal-Organic Frameworks and their Composites for Energy Storage and Conversion, *Adv. Mater.*, 2018, **30**, 1702891.
23 G. Yilmaz, S. B. Peh, D. Zhao and G. W. Ho, Atomic- and Molecular-Level Design of Functional Metal-Organic Frameworks (MOFs) and Derivatives for Energy and Environmental Applications, *Adv. Sci.*, 2019, **6**, 1901129.
24 S. Zhao, Y. Wang, J. Dong, C.-T. He, H. Yin, P. An, K. Zhao, X. Zhang, C. Gao, L. Zhang, J. Lv, J. Wang, J. Zhang, A. M. Khattak, N. A. Khan, Z. Wei, J. Zhang, S. Liu, H. Zhao and Z. Tang, Ultrathin metal–organic framework nanosheets for electrocatalytic oxygen evolution, *Nat. Energy*, 2016, **1**, 16184.
25 P. Thangavel, M. Ha, S. Kumaraguru, A. Meena, A. N. Singh, A. M. Harzandi and K. S. Kim, Graphene-nanoplatelets-supported NiFe-MOF: high-efficiency and ultra-stable oxygen electrodes for sustained alkaline anion exchange membrane water electrolysis, *Energy Environ. Sci.*, 2020, **13**, 3447–3458.
26 F. L. Li, Q. Shao, X. Huang and J. P. Lang, Nanoscale Trimetallic Metal-Organic Frameworks Enable Efficient Oxygen Evolution Electrocatalysis, *Angew. Chem., Int. Ed.*, 2018, **57**, 1888–1892.
27 D. Zhu, M. Qiao, J. Liu, T. Tao and C. Guo, Engineering pristine 2D metal–organic framework nanosheets for electrocatalysis, *J. Mater. Chem. A*, 2020, **8**, 8143–8170.
28 S. Jin, How to Effectively Utilize MOFs for Electrocatalysis, *ACS Energy Lett.*, 2019, **4**, 1443–1445.
29 F. L. Li, P. Wang, X. Huang, D. J. Young, H. F. Wang, P. Braunstein and J. P. Lang, Large-Scale, Bottom-Up Synthesis of Binary Metal-Organic Framework Nanosheets for Efficient Water Oxidation, *Angew. Chem., Int. Ed.*, 2019, **58**, 7051–7056.
30 M. Zhao, Q. Lu, Q. Ma and H. Zhang, Two-Dimensional Metal-Organic Framework Nanosheets, *Small Methods*, 2017, **1**, 1600030.
31 G. Hai, X. Jia, K. Zhang, X. Liu, Z. Wu and G. Wang, High-performance oxygen evolution catalyst using two-dimensional ultrathin metal-organic frameworks nanosheets, *Nano Energy*, 2018, **44**, 345–352.
32 M. Zhao, Y. Huang, Y. Peng, Z. Huang, Q. Ma and H. Zhang, Two-dimensional metal-organic framework nanosheets: synthesis and applications, *Chem. Soc. Rev.*, 2018, **47**, 6267–6295.
33 W. Liu, R. Yin, X. Xu, L. Zhang, W. Shi and X. Cao, Structural Engineering of Low–Dimensional Metal–Organic Frameworks: Synthesis, Properties, and Applications, *Adv. Sci.*, 2019, **6**, 1802373.
34 J. Du, F. Li and L. Sun, Metal-organic frameworks and their derivatives as electrocatalysts for the oxygen evolution reaction, *Chem. Soc. Rev.*, 2021, **50**, 2663–2695.
35 J. Duan, S. Chen and C. Zhao, Ultrathin metal-organic framework array for efficient electrocatalytic water splitting, *Nat. Commun.*, 2017, **8**, 15341.
36 F. Dionigi and P. Strasser, NiFe-Based (Oxy)hydroxide Catalysts for Oxygen Evolution Reaction in Non-Acidic Electrolytes, *Adv. Energy Mater.*, 2016, **6**, 1600621.
37 X. Long, Z. Wang, S. Xiao, Y. An and S. Yang, Transition metal based layered double hydroxides tailored for energy conversion and storage, *Mater. Today*, 2016, **19**, 213–226.
38 Q. Xiang, F. Li, W. Chen, Y. Ma, Y. Wu, X. Gu, Y. Qin, P. Tao, C. Song, W. Shang, H. Zhu, T. Deng and J. Wu, In Situ Vertical Growth of Fe–Ni Layered Double-Hydroxide Arrays on Fe–Ni Alloy Foil: Interfacial Layer Enhanced Electrocatalyst with Small Overpotential for Oxygen Evolution Reaction, *ACS Energy Lett.*, 2018, **3**, 2357–2365.
39 R. Chen, S. F. Hung, D. Zhou, J. Gao, C. Yang, H. Tao, H. B. Yang, L. Zhang, L. Zhang, Q. Xiong, H. M. Chen and B. Liu, Layered Structure Causes Bulk NiFe Layered Double Hydroxide Unstable in Alkaline Oxygen Evolution Reaction, *Adv. Mater.*, 2019, **31**, e1903909.
40 H.-Y. Wang, Y.-Y. Hsu, R. Chen, T.-S. Chan, H. M. Chen and B. Liu, Ni^{3+}-Induced Formation of Active NiOOH on the Spinel Ni–Co Oxide Surface for Efficient Oxygen Evolution Reaction, *Adv. Energy Mater.*, 2015, **5**, 15000911.
41 W.-J. Liu, L. Dang, Z. Xu, H.-Q. Yu, S. Jin and G. W. Huber, Electrochemical Oxidation of 5-Hydroxymethylfurfural with NiFe Layered Double Hydroxide (LDH) Nanosheet Catalysts, *ACS Catal.*, 2018, **8**, 5533–5541.
42 B. Wang, J. Shang, C. Guo, J. Zhang, F. Zhu, A. Han and J. Liu, A General Method to Ultrathin Bimetal-MOF Nanosheets Arrays via In Situ Transformation of Layered Double Hydroxides Arrays, *Small*, 2019, **15**, e1804761.
43 W. Cheng, X. F. Lu, D. Luan and X. W. D. Lou, NiMn-Based Bimetal-Organic Framework Nanosheets Supported on Multi-Channel Carbon Fibers for Efficient Oxygen Electrocatalysis, *Angew. Chem., Int. Ed.*, 2020, **59**, 18234–18239.
44 B. M. Hunter, W. Hieringer, J. R. Winkler, H. B. Gray and A. M. Müller, Effect of interlayer anions on [NiFe]-LDH nanosheet water oxidation activity, *Energy Environ. Sci.*, 2016, **9**, 1734–1743.
45 Y. Liu, N. Wang, J. H. Pan, F. Steinbach and J. Caro, In situ synthesis of MOF membranes on ZnAl-CO_3 LDH buffer layer-modified substrates, *J. Am. Chem. Soc.*, 2014, **136**, 14353–14356.

46 J. A. Carrasco, G. Abellán and E. Coronado, Influence of morphology in the magnetic properties of layered double hydroxides, *J. Mater. Chem. C*, 2018, **6**, 1187–1198.
47 X. J. Bai, X. Y. Lu, R. Ju, H. Chen, L. Shao, X. Zhai, Y. N. Li, F. Q. Fan, Y. Fu and W. Qi, Preparation of MOF Film/Aerogel Composite Catalysts via Substrate-Seeding Secondary-Growth for the Oxygen Evolution Reaction and CO_2 Cycloaddition, *Angew. Chem., Int. Ed.*, 2021, **60**, 701–705.
48 L. Huang, G. Gao, H. Zhang, J. Chen, Y. Fang and S. Dong, Self-dissociation-assembly of ultrathin metal-organic framework nanosheet arrays for efficient oxygen evolution, *Nano Energy*, 2020, **68**, 104296.
49 Z. Liu, R. Ma, M. Osada, N. Iyi, Y. Ebina, K. Takada and T. Sasaki, Synthesis, Anion Exchange, and Delamination of Co–Al Layered Double Hydroxide: Assembly of the Exfoliated Nanosheet/Polyanion Composite Films and Magneto-Optical Studies, *J. Am. Chem. Soc.*, 2006, **128**, 4872–4880.
50 K. I. Hadjiivanov, D. A. Panayotov, M. Y. Mihaylov, E. Z. Ivanova, K. K. Chakarova, S. M. Andonova and N. L. Drenchev, Power of Infrared and Raman Spectroscopies to Characterize Metal-Organic Frameworks and Investigate Their Interaction with Guest Molecules, *Chem. Rev.*, 2021, **121**, 1286–1424.
51 F. Sun, G. Wang, Y. Ding, C. Wang, B. Yuan and Y. Lin, NiFe-Based Metal-Organic Framework Nanosheets Directly Supported on Nickel Foam Acting as Robust Electrodes for Electrochemical Oxygen Evolution Reaction, *Adv. Energy Mater.*, 2018, **8**, 1800584.
52 J. Li, W. Huang, M. Wang, S. Xi, J. Meng, K. Zhao, J. Jin, W. Xu, Z. Wang, X. Liu, Q. Chen, L. Xu, X. Liao, Y. Jiang, K. A. Owusu, B. Jiang, C. Chen, D. Fan, L. Zhou and L. Mai, Low-Crystalline Bimetallic Metal–Organic Framework Electrocatalysts with Rich Active Sites for Oxygen Evolution, *ACS Energy Lett.*, 2018, **4**, 285–292.
53 S. Bordiga, C. Lamberti, G. Ricchiardi, L. Regli, F. Bonino, A. Damin, K. P. Lillerud, M. Bjorgen and A. Zecchina, Electronic and vibrational properties of a MOF-5 metal-organic framework: ZnO quantum dot behaviour, *Chem. Commun.*, 2004, 2300–2301, DOI: **10.1039/b407246d**.
54 D. Zhu, C. Guo, J. Liu, L. Wang, Y. Du and S. Z. Qiao, Two-dimensional metal-organic frameworks with high oxidation states for efficient electrocatalytic urea oxidation, *Chem. Commun.*, 2017, **53**, 10906–10909.
55 H. Chen, Z. Shen, Z. Pan, Z. Kou, X. Liu, H. Zhang, Q. Gu, C. Guan and J. Wang, Hierarchical Micro-Nano Sheet Arrays of Nickel-Cobalt Double Hydroxides for High-Rate Ni-Zn Batteries, *Adv. Sci.*, 2019, **6**, 1802002.
56 L. Cai, J. Zhao, H. Li, J. Park, I. S. Cho, H. S. Han and X. Zheng, One-Step Hydrothermal Deposition of Ni:FeOOH onto Photoanodes for Enhanced Water Oxidation, *ACS Energy Lett.*, 2016, **1**, 624–632.
57 Q. Zhou, Y. Chen, G. Zhao, Y. Lin, Z. Yu, X. Xu, X. Wang, H. K. Liu, W. Sun and S. X. Dou, Active-Site-Enriched Iron-Doped Nickel/Cobalt Hydroxide Nanosheets for Enhanced Oxygen Evolution Reaction, *ACS Catal.*, 2018, **8**, 5382–5390.
58 C. Wu, H. Li, Z. Xia, X. Zhang, R. Deng, S. Wang and G. Sun, NiFe Layered Double Hydroxides with Unsaturated Metal Sites via Precovered Surface Strategy for Oxygen Evolution Reaction, *ACS Catal.*, 2020, **10**, 11127–11135.
59 Q. Zhang, N. M. Bedford, J. Pan, X. Lu and R. Amal, A Fully Reversible Water Electrolyzer Cell Made Up from FeCoNi (Oxy)hydroxide Atomic Layers, *Adv. Energy Mater.*, 2019, **9**, 1901312.
60 W. Li, F. Li, H. Yang, X. Wu, P. Zhang, Y. Shan and L. Sun, A bio-inspired coordination polymer as outstanding water oxidation catalyst via second coordination sphere engineering, *Nat. Commun.*, 2019, **10**, 5074.
61 C. Xia, Q. Jiang, C. Zhao, M. N. Hedhili and H. N. Alshareef, Selenide-Based Electrocatalysts and Scaffolds for Water Oxidation Applications, *Adv. Mater.*, 2016, **28**, 77–85.
62 Y. Wang, M. Qiao, Y. Li and S. Wang, Tuning Surface Electronic Configuration of NiFe LDHs Nanosheets by Introducing Cation Vacancies (Fe or Ni) as Highly Efficient Electrocatalysts for Oxygen Evolution Reaction, *Small*, 2018, **14**, 1800136.